Cross-sectional imaging of individual layers and buried interfaces of graphene-based heterostructures and superlattices

S. J. Haigh[1]★, A. Gholinia[1], R. Jalil[2], S. Romani[3], L. Britnell[2], D. C. Elias[2], K. S. Novoselov[2], L. A. Ponomarenko[2], A. K. Geim[2] and R. Gorbachev[2]★

By stacking various two-dimensional (2D) atomic crystals[1] on top of each other, it is possible to create multilayer heterostructures and devices with designed electronic properties[2–5]. However, various adsorbates become trapped between layers during their assembly, and this not only affects the resulting quality but also prevents the formation of a true artificial layered crystal upheld by van der Waals interaction, creating instead a laminate glued together by contamination. Transmission electron microscopy (TEM) has shown that graphene and boron nitride monolayers, the two best characterized 2D crystals, are densely covered with hydrocarbons (even after thermal annealing in high vacuum) and exhibit only small clean patches suitable for atomic resolution imaging[6–10]. This observation seems detrimental for any realistic prospect of creating van der Waals materials and heterostructures with atomically sharp interfaces. Here we employ cross sectional TEM to take a side view of several graphene–boron nitride heterostructures. We find that the trapped hydrocarbons segregate into isolated pockets, leaving the interfaces atomically clean. Moreover, we observe a clear correlation between interface roughness and the electronic quality of encapsulated graphene. This work proves the concept of heterostructures assembled with atomic layer precision and provides their first TEM images.

Top-view TEM of graphene and boron nitride monolayers has allowed visualization and analysis of various types of defects, including ripples, vacancies, substitutional atoms, adatoms, grain boundaries and edges[6–14]. Elemental analysis at the level of individual atoms can now be achieved by means of annular dark-field imaging[15], electron energy-loss (EEL) spectroscopy[7,9,10,16,17] or energy dispersive X-ray (EDX) spectroscopy[18]. These atomic-scale insights are important for fundamental and technological progress in this research area because defects determine the electronic quality of graphene devices[19] and can lead to pinholes in tunnel barriers[20–22].

Most recently, the field has expanded beyond studying graphene and isolated 2D crystals. There is a rapidly growing interest in atomic-scale heterostructures made from a combination of alternating layers of graphene, hexagonal boron-nitride (hBN), MoS_2 and so on. Such heterostructures provide a higher electronic quality for lateral graphene devices[23,24] and, also, allow a conceptually new degree of flexibility in designing electronic, optoelectronic, micromechanical and other devices[2–5]. New fundamental physics not present for individual 2D crystals is widely expected to emerge in heterostructures with atomically thin barriers and quantum wells[3,25]. However, defects and, in particular, adsorbates trapped between 2D crystals can diminish their quality. In the case of multilayer structures, their top-view TEM images are difficult or impossible to interpret because many different layers are superimposed in projection. Conventional surface-analysis techniques are also insensitive to the buried interfaces and trapped contamination. To obtain information about such atomic-scale heterostructures, a different approach is necessary.

In this Letter, we have studied multilayer heterostructure devices in which mono- and bilayer graphene crystals were individually contacted and interlaid between atomically thin hBN crystals. After microfabrication (see Methods) and electron transport measurements, TEM specimens were extracted from the studied devices as follows. A suitable region for side-view imaging was chosen by using optical and scanning electron microscopy (SEM; Fig. 1). An Au–Pd film (50 nm thick) was then sputtered onto the whole surface, followed by a narrow Pt strap (1 μm thick) deposited over the region of interest. The metal layers served to prevent charging and protect the selected region from ion damage. Focused ion beam (FIB) milling was then used to produce a cross-sectional slice under the Pt strap. The slice was then transferred and attached to a TEM grid, a sample preparation approach known as the lift-out method[26,27]. Finally, we employed low-energy ion milling to thin the extracted slices down to 20–70 nm so that they could be analysed at high resolution by scanning TEM (STEM) (refs 28,29).

Figure 1 shows one of our investigated devices and its step-by-step preparation for STEM. The particular device consists of monolayer graphene placed on top of a relatively thick (30 nm) hBN crystal, covered with a few-layer hBN spacer and then another graphene sheet on top (Fig. 1a). A cross-sectional specimen extracted from the device is shown in Fig. 1d. At this low magnification only the Pt protective layer and Si substrate are visible. Individual atomic layers become clearly resolved by using high-resolution STEM. One can easily count them in Fig. 1e. In this projection, little difference is expected between graphene and hBN atomic planes but our images consistently show two regions of slightly reduced contrast and intensity, which coincide with the expected positions of the two graphene sheets, above and below the hBN spacer. We attribute this to the higher susceptibility of graphene or the interfaces to ion beam damage. The dips in contrast allow us to estimate the hBN spacer thickness, d, as four atomic layers, in agreement with atomic force microscopy (AFM)

[1]School of Materials, University of Manchester, Manchester M13 9PL, UK, [2]Manchester Centre for Mesoscience and Nanotechnology, University of Manchester, Manchester M13 9PL, UK, [3]Department of Engineering, University of Liverpool, Liverpool L69 3GH, UK.
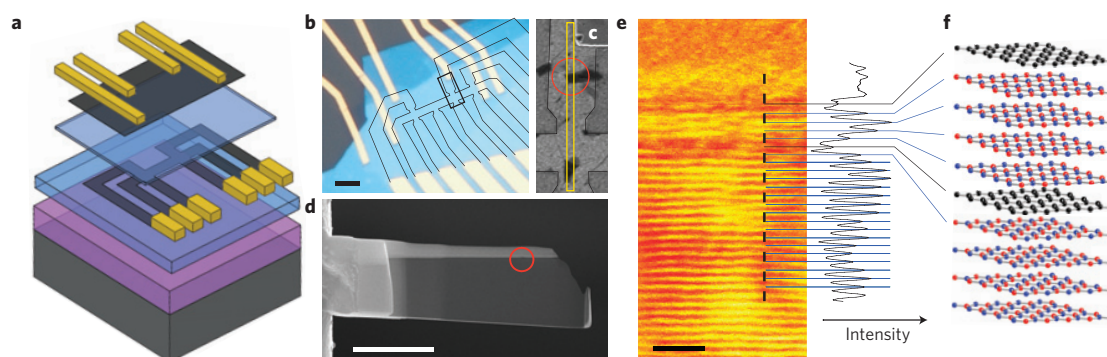*e-mail: sarah.haigh@manchester.ac.uk; blizza@gmail.com.

Figure 1 | Cross-sectional TEM of graphene–hBN heterostructures. a, Schematic of one of our devices: two graphene monolayers (dark grey) are interlaid with hBN crystals (blue) and have separate electrical contacts (yellow). The heterostructure is fabricated on top of an oxidized silicon wafer (violet and grey). **b**, Optical image of the device before extracting a cross-sectional sample. The graphene Hall bar is highlighted with thin black lines. The black rectangle (1.8 μm × 4.4 μm) indicates the area enlarged in the SEM micrograph (**c**), in which the yellow rectangle marks the region chosen for our study. **d**, Low-magnification SEM image of the final cross-sectional slice for TEM imaging. Red circles in **c,d** indicate a 'bubble' of trapped adsorbates. **e**, High-resolution bright-field aberration-corrected STEM image of the graphene–hBN heterostructure in the circled region. **f**, Averaged line scan of the intensity along the dashed black line in **e** (total length 9.4 nm, integration width 2 nm) with a schematic of the atomic layer sequence for this particular device shown on the right, in which carbon, boron and nitrogen atoms are represented as black, blue and red respectively. Scale bars in **b** and **d** are 3 μm. Scale bar in **e** is 2 nm.

measurements during fabrication of the device ($d \approx 1$–2 nm) and its tunnelling characteristics yielding $d = 4$ hBN layers[22].

Because the individual crystals are prepared under ambient conditions, various chemical species get absorbed on their surfaces, as commonly seen by SEM and top-view TEM (refs 6–10). Note that AFM and scanning tunnelling microscopy usually do not 'see' this contamination, probably because it is easily moved by the tip. During fabrication of our heterostructures, the contamination layer is expected to remain between the layers. In this work, we find that adsorbates tend to diffuse over micrometre scale distances and form relatively large (μm) pockets of the trapped material, which are clearly seen as 'bubbles' in an optical microscope and as dark spots in SEM (Fig. 1c and Supplementary Information). These inhomogeneities can be detrimental to device performance and decrease graphene's carrier mobility, μ. To avoid this, we normally heated our devices to 300 °C to enhance the diffusion. This helped to obtain clean, atomically flat areas large enough to fabricate graphene devices of a micrometre width with no bubbles within the active area (see Supplementary Information for our studies on bubbles' morphology). To find out what is inside the bubbles, so as to identify their chemistry and origins, we have deliberately chosen in Fig. 1 to image a cross-section that goes through one of the bubbles. Another example is shown in Fig. 2, where a low-magnification image provides a better view of the contamination bubble. The bubble contains an amorphous material that is trapped between the top graphene layer (G_T) and hBN spacer (BN_T) and becomes hardened, probably during ion milling (Supplementary Information). Chemical analysis using EDX and EEL spectroscopy has revealed that the trapped contaminants are mostly hydrocarbons (Fig. 2b).

The acquired cross-sectional EEL spectra also allow us to chemically identify approximate locations of the graphene layers. Indeed, Fig. 2b shows a drop in the BN signal and a simultaneous increase in the carbon signal (note that on this particular image G_T is absent, being lifted away by hydrocarbon contamination). The limited resolution (≈ 1 nm) of our elemental mapping in Fig. 2b is consistent with the spreading of the focused electron probe, which can be estimated from the thickness of the cross-sectional slice (≈ 40 nm) and the employed 20 mrad convergence angle[30]. For the device in Fig. 2 the EEL spectroscopy yields $d = 4$–5 nm for BN_T, in agreement with the device's AFM characterization and its quantum capacitance measurements[3]. For such relatively thick hBN spacers,
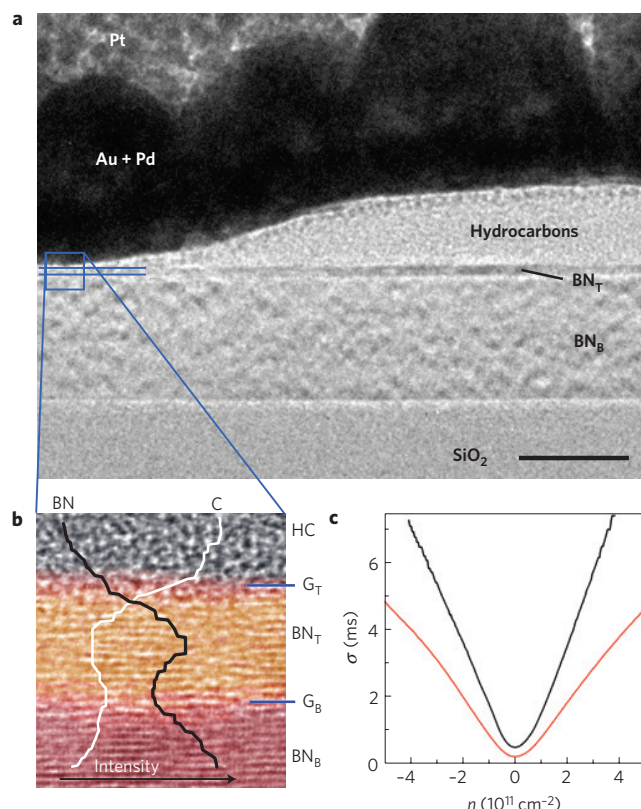

Figure 2 | Characterization of chemical species trapped between layers. a, Bright-field TEM image showing the top part of the oxidized Si wafer, BN substrate layer (BN_B), BN spacer (BN_T), hydrocarbon residue (HC) and metallic coating (Au–Pd layer + Pt strap). Scale bar, 25 nm. **b**, Bright-field aberration-corrected STEM image of an enlarged region of the same heterostructure. Superimposed are elemental profiles for the carbon-K edge and boron-K edge extracted from EEL spectra acquired sequentially in the STEM mode. The peak in the C content for the G_B corresponds to a maximum relative atomic composition of 55%. The image is 10 nm wide. **c**, Electrical characterization of graphene layers in this device. Conductivity σ of top (red) and bottom (black) graphene as a function of carrier density n. The larger the slope of $\sigma(n)$, the higher graphene's μ.
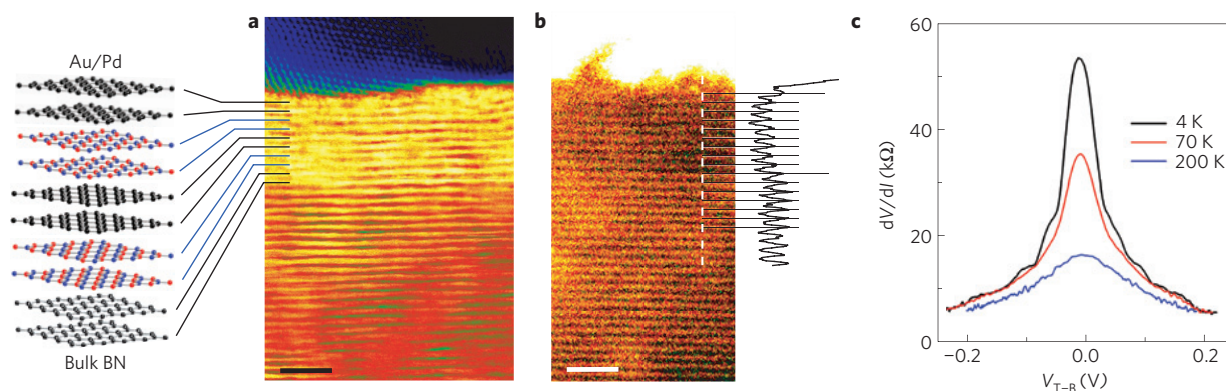
Figure 3 | Graphene–BN superlattice. a, Bright-field cross sectional STEM of a stack of graphene and hBN bilayers with the layer sequence schematically shown to the left. **b**, HAADF STEM image of the same superlattice with an intensity line profile of length 7 nm and integration width 5 nm plotted to the right. **c**, Vertical transport through the superlattice. Current, I, was measured as a function of bias voltage, V_{T-B}, applied between the top and bottom graphene bilayers. The differential resistance dV/dI exhibits a zero-bias peak that grows with decreasing temperature. Scale bars, 2 nm.

the BN_T and BN_B layers are often observed to have different contrast in the medium-angle annular dark-field STEM images (shown in false colour in Fig. 2b; $d \approx 4.5$ nm), which is attributed to these hBN crystals having different lattice orientations, with the BN_T rotated about the c axis relative to BN_B.

The isolated pockets of trapped hydrocarbons are of concern for fabrication and possible lateral sizes of graphene–hBN heterostructures but even more serious is the question of whether such contamination remains at the interfaces in a sub-monolayer thickness, which can affect their electronic quality and smoothness. We address this issue by analysing our high-resolution TEM images. To this end, we have used an analysis of peak positions in the intensity spectra (such as in Fig. 1f) to accurately measure interlayer distances (see Supplementary Information). We find that within experimental accuracy the spacing between hBN and graphene planes is indistinguishable from the basal plane separation in bulk hBN (for the device in Fig. 1 our accuracy given by a standard deviation Δ was ≈ 0.07 nm). This suggests that the interface between graphene and hBN cannot contain more than a small fraction of a monolayer of adsorbates, that is, the interface is practically clean and atomically sharp.

Furthermore, we have estimated the roughness of each atomic layer in our TEM images by analysing the standard deviation of intensity peak positions from a straight line (Supplementary Information). This analysis reveals a significant difference in the average roughness δ between the top and bottom graphene planes ($\delta \approx 0.072$ and 0.038 nm for G_T and bottom graphene layer (G_B), respectively, for the device in Fig. 1). For comparison, atomic planes within BN_T and BN_B yield the same δ as G_B, with the same experimental error of ± 0.023 nm. We believe that, despite the use of low-energy ion polishing and short dwell times during STEM imaging, the background level of roughness can be due to beam damage. This does not account for the three times higher δ for the G_T. Moreover, the observed roughness correlates with graphene's electronic quality, so that G_T and G_B exhibited $\mu \approx 60{,}000$ and $120{,}000$ cm^2 V^{-1} s^{-1}, respectively, for the device in Fig. 2c. Lower μ in G_T was a systematic effect observed for all our devices. We speculate that the difference in μ is a result of stronger rippling[31] for the unprotected top graphene or of more adsorbates trapped at the top interface. In either case, this observation shows that the encapsulation is important for achieving atomically flat and high-μ graphene, in agreement with results of ref. 24.

Presented in Fig. 3 is an example of a more sophisticated heterostructure, comprised of several graphene bilayers separated by hBN bilayers. Fabrication of this device required sequential deposition of many crystals on top of each other (we made devices with up to 10 different layers). AFM and optical characterization of each bilayer before the assembly have assured the exact heterostructure composition as designed. For the device in Fig. 3, its high-resolution bright-field and high-angle annular dark-field (HAADF) imaging reveal a region of different contrast for the ten atomic layers representing the superlattice region. Compositional analysis using EEL spectroscopy shows a systematic increase in the carbon K-edge signal within this region but is unable to identify the individual graphene bilayers because the resolution is limited to ~1 nm. Analysis of the intensity profiles extracted from HAADF STEM images (like that shown in Fig. 3b) reveals a spacing for the hBN-graphene superlattice of $\approx 0.332 \pm 0.043$ nm, equal to the interlayer distance in bulk hBN (measured to be ≈ 0.326 nm, with the same accuracy for the upper part of the BN substrate). No systematic change in lattice separation was observed as a function of distance from the hBN substrate (Supplementary Information). These measurements prove again that the graphene/hBN interfaces become atomically clean due to the segregation of adsorbed hydrocarbons.

The structural TEM studies also aid interpretation of electron transport measurements. For the described graphene-BN superlattice, metallic contacts were attached to the top and bottom graphene bilayers to probe electrical conductivity in the vertical direction. Figure 3c shows the differential resistivity for the same superlattice as imaged in Fig. 3a,b. The measured I–V characteristics are strongly nonlinear because hBN bilayers act as tunnel barriers, in agreement with the recent studies of tunnelling through individual hBN crystals[20–22]. On the other hand, the nonlinearity appears in the superlattice at biases as small as <10 meV and the zero-bias peak grows by a factor of five between room and liquid-helium temperatures. This behaviour is inconsistent with that observed for individual hBN bilayers[22]. Its full interpretation is beyond the scope of this Letter. Let us only mention that we attribute the zero-bias peak to a combination of two effects: a decrease in the tunnelling density of states at the neutrality point in bilayer graphene as temperature decreases and a 'zero-bias anomaly' that can appear due to the interaction of a tunnelling electron with a virtual hole left behind in a 2D electronic system[32].

In conclusion, our high-resolution images show that new kinds of heterostructures with atomically sharp interfaces can be assembled in various combinations from the available library of 2D crystals. It is highly nontrivial that the contamination inevitably present on top of 2D crystals and trapped during their assembly segregates into isolated pockets, leaving the buried interfaces clean and atomically flat. Moreover, our work shows that cross-sectional TEM can be a useful tool to aid interpretation

of transport measurements and therefore further progress in graphene-based electronics, allowing side-view characterization with atomic resolution.

Methods

Fabrication of multilayer heterostructure devices. The stack begins with a thick (~50 nm) hBN flake deposited on top of an oxidized Si wafer. Each subsequent layer is prepared on a separate wafer, delaminated from the surface and transferred on top of the target crystal. The freshly deposited layer can then be shaped by reactive plasma etching and annealed (300° C in Ar/H_2) to remove processing residues. Because the graphene layers are interlaid by insulating hBN spacers, each of them can be separately connected (we used Au/Ti contacts) and studied independently. More details on device fabrication can be found in ref. 3. For further information on contamination pockets (bubbles), see Supplementary Information.

Preparation of TEM samples. A dual-beam instrument (FEI Nova NanoLab 600) has been used for site-specific preparation of cross-sectional samples suitable for TEM analysis using the lift-out approach[26–29]. This instrument combines a FIB and a SEM column in the same chamber and is also fitted with a gas-injection system to allow local material deposition and material-specific preferential milling to be performed by introducing reactive gases in the vicinity of the electron or ion probe. The electron column delivers the imaging abilities of the SEM and is at the same time less destructive than FIB imaging. SEM imaging of the device before milling allows one to identify an area suitable for side-view imaging. After sputtering of a 50 nm Au–Pd coating on the whole surface *ex situ*, the Au/Ti contacts on graphene were still visible as raised regions in the secondary electron image. These were used to correctly position the ion beam so that a Pt strap layer could be deposited on the surface at a chosen location, increasing the metallic layer above the device to ~1 μm. The strap protects the region of interest during milling as well as providing mechanical stability to the cross-sectional slice after its removal. Trenches were milled around the strap by using a 30 kV Ga^+ beam with a current of 0.1–5 nA. Before removing the final edge supporting the milled slice and milling beneath it to free it from the substrate, one end of the Pt strap slice was welded to a nanomanipulator needle using further Pt deposition. The cross-sectional slice with typical dimensions of 1 μm × 5 μm × 10 μm could then be extracted and transferred to an Omniprobe copper half grid, as required for TEM. The slice was then welded onto the grid using further Pt deposition so that it could be safely separated from the nanomanipulator by FIB milling. A final gentle polish with Ga^+ ions (at 5 kV and 50 pA) was used to remove side damage and reduce the specimen thickness to 20–70 nm, as measured using energy filtered TEM. The fact that the cross-sectional slice was precisely extracted from the chosen spot was confirmed for all devices by comparing the positions of identifiable features such as Au contacts and/or hydrocarbon bubbles, which are visible both in the SEM images of the original device and within TEM images of the prepared cross-section (see, for example, Fig. 1).

TEM and image analysis. TEM imaging was carried out using a Tecnai F30 FEG-TEM operated at 300 kV and equipped with an EDX detector. STEM imaging was performed by using a probe-side aberration-corrected JEOL 2100F operated at 200 kV with the third-order spherical aberration set to zero (±5 μm). The multilayer structures were oriented along an ⟨hkl0⟩ crystallographic direction by taking advantage of the Kikuchi bands of the Si substrate. Images were collected using a convergence angle of 20 mrad and a high angle annular dark-field (HAADF) detector with an inner (outer) collection angle of 74 (196) mrad. EEL spectroscopy data was acquired using a quantum Gatan imaging filter and a collection angle of 24 mrad. Analysis of the EELS line scan data was performed using Digital Micrograph software with pre- and post-edge windows of ~20 eV.

Analysis of the local interlayer separation and layer roughness was performed using line profiles extracted from the images within the Semper image processing software. Details of the analysis are provided in the Supplementary Information.

References

1. Novoselov, K. S. *et al.* Two-dimensional atomic crystals. *Proc. Natl Acad. Sci. USA* **102,** 10451–10453 (2005).
2. Wang, H. *et al.* BN/Graphene/BN transistors for RF applications. *IEEE Electron Device Lett.* **32,** 1209–1211 (2011).
3. Ponomarenko, L. A. *et al.* Tunable metal-insulator transition in double-layer graphene heterostructures. *Nature Phys.* **7,** 958–961 (2011).
4. Britnell, L. *et al.* Field-effect tunneling transistor based on vertical graphene heterostructures. *Science* **335,** 947–950 (2012).
5. Yankowitz, M. *et al.* Emergence of superlattice Dirac points in graphene on hexagonal boron nitride. *Nature Phys.* **8,** 382–386 (2012).
6. Meyer, J. C. *et al.* The structure of suspended graphene sheets. *Nature* **446,** 60–63 (2007).
7. Gass, M. H. *et al.* Free-standing graphene at atomic resolution. *Nature Nanotech.* **3,** 676–681 (2008).
8. Ci, L. *et al.* Atomic layers of hybridized boron nitride and graphene domains. *Nature Mater.* **9,** 430–435 (2010).
9. Pan, C. T. *et al.* Nanoscale electron diffraction and plasmon spectroscopy of single- and few-layer boron nitride. *Phys. Rev. B* **85,** 045440 (2012).
10. Zhou, W. *et al.* Atomically localized plasmon enhancement in monolayer graphene. *Nature Nanotech.* **7,** 161–165 (2012).
11. Hashimoto, A. *et al.* Direct evidence for atomic defects in graphene layers. *Nature* **430,** 870–873 (2004).
12. Warner, J. H. *et al.* Structural transformations in graphene studied with high spatial and temporal resolution. *Nature Nanotech.* **4,** 500–504 (2009).
13. Robertson, A. W. *et al.* Atomic structure of interconnected few layer graphene domains. *ACS Nano* **5,** 6610–6618 (2011).
14. Meyer, J. C. *et al.* Experimental analysis of charge redistribution due to chemical bonding by high-resolution transmission electron microscopy. *Nature Mater.* **10,** 209–215 (2011).
15. Krivanek, O. L. *et al.* Atom-by-atom structural and chemical analysis by annular dark-field electron microscopy. *Nature* **464,** 571–574 (2010).
16. Suenaga, K. & Koshino, M. Atom-by-atom spectroscopy at graphene edge. *Nature* **468,** 1088–1090 (2010).
17. Zan, R. *et al.* Metal–graphene interaction studied via atomic resolution scanning transmission electron microscopy. *Nano Lett.* **11,** 1087–1092 (2012).
18. Lovejoy, T. C. *et al.* Single atom identification by energy dispersive x-ray spectroscopy. *Appl. Phys. Lett.* **100,** 154101 (2012).
19. Castro Neto, A. H., Guinea, F., Peres, N. M. R., Novoselov, K. S. & Geim, A. K. The electronic properties of graphene. *Rev. Mod. Phys.* **81,** 109–162 (2009).
20. Amet, F. *et al.* Tunneling spectroscopy of graphene–boron–nitride heterostructures. *Phys. Rev. B* **85,** 073405 (2012).
21. Lee, G. H. *et al.* Electron tunneling through atomically flat and ultrathin hexagonal boron nitride. *Appl. Phys. Lett.* **99,** 243114 (2011).
22. Britnell, L. *et al.* Atomically thin boron nitride: A tunneling barrier for graphene devices. *Nano Lett.* **12,** 1707–1710 (2012).
23. Dean, C. R. *et al.* Boron nitride substrates for high-quality graphene electronics. *Nature Nanotech.* **5,** 722–726 (2010).
24. Mayorov, A. S. *et al.* Micrometer-scale ballistic transport in encapsulated graphene at room temperature. *Nano Lett.* **11,** 2396–2399 (2011).
25. Min, H., Bistritzer, R., Su, J. J. & MacDonald, A. H. Room-temperature superfluidity in graphene bilayers. *Phys. Rev. B* **78,** 121401 (2008).
26. Giannuzzi, L. A. & Stevie, F. A. A review of focused ion beam milling techniques for TEM specimen preparation. *Micron* **30,** 197–204 (1999).
27. Langford, R. M. Focused ion beams techniques for nanomaterials characterization. *Microscopy Res. Tech.* **69,** 538–549 (2006).
28. Schaffer, M. *et al.* Sample preparation for atomic-resolution STEM at low voltages by FIB. *Ultramicroscopy* **114,** 62–71 (2012).
29. Rubanov, S. & Munroe, P. R. Investigation of the structure of damage layers in TEM samples prepared using a focused ion beam. *J. Mater. Sci. Lett.* **20,** 1181–1183 (2001).
30. Suenaga, K. *et al.* Synthesis of nanoparticles and nanotubes with well-separated layers of boron nitride and carbon. *Science* **278,** 653–655 (1997).
31. Katsnelson, M. I. & Geim, A. K. Electron scattering on microscopic corrugations in graphene. *Phil. Trans. R. Soc. A* **366,** 195–204 (2008).
32. Altshuler, B. L. & Aronov, A. G. Zero bias anomaly in tunnel resistance and electron–electron interaction. *Solid State Commun.* **30,** 115–117 (1979).

Author contributions

S.J.H. and R.G. led the project. Devices were made by R.G. and R.J. with electrical characterization by L.A.P., D.C.E. and K.S.N. S.J.H. performed TEM imaging and analysis. A.G. operated the FIB and S.R. provided TEM instrumental support. L.B. performed AFM analysis. R.G., S.J.H. and A.K.G. wrote the paper. All authors carried out data analysis, participated in discussion of the results and commented on the manuscript.

Additional information

Supplementary information is available in the online version of the paper. Reprints and permissions information is available online at www.nature.com/reprints. Correspondence and requests for materials should be addressed to S.J.H. or R.G.

Competing financial interests

The authors declare no competing financial interests.